Microscopic and conventional optical model analysis of fast neutron scattering from ^{54,56}Fe

S. Mellema and R. W. Finlay
Department of Physics, Ohio University, Athens, Ohio 45701

F. S. Dietrich
Lawrence Livermore National Laboratory, Livermore, California 94550

F. Petrovich
Department of Physics, Florida State University, Tallahassee, Florida 32306
(Received 23 May 1983)

Differential cross sections for elastic scattering of neutrons from ^{54,56}Fe have been measured at several energies in the 20—26 MeV region. The data have been analyzed both in terms of the standard phenomenological optical model, and in the framework of two different microscopic models based upon nuclear matter calculations using realistic nucleon-nucleon interactions and a local density approximation. Isospin consistency of the microscopic-model calculations was also tested by analyzing proton elastic differential cross section data in the same energy region, as well as both proton and neutron elastic analyzing power data. The microscopic calculations yield quite reasonable agreement with the data, even though they contain no free geometrical parameters. The quality of the results for the analyzing power data is particularly impressive, indicating that the very simple, density- and energy-independent spin-orbit force used in the calculations is sufficient. The differences between the various models are clarified by examining the momentum-space representations of the potentials.

[NUCLEAR REACTIONS ^{54}Fe(n,n) E_n=20, 22, 24, and 26 MeV, ^{56}Fe(n,n) E_n=20, 26 MeV. Measured $(d\sigma/d\Omega)(\theta)$. Calculated optical model potentials. Microscopic analysis.]

I. INTRODUCTION

Much effort has been expended in the past decade in analyzing neutron elastic scattering differential cross section data in terms of optical model potentials.[1] Most of this analysis has been phenomenological in nature, assuming standard form factors for the potentials and then fitting the data by varying a number of parameters. Reasonable success has also been obtained by so-called "global" analyses which, by fitting many data sets over a wide energy and mass range with the procedure described above, find average parameters for form factors and reasonable energy dependences for potential depths.[2,3]

However, the advent of a capability to measure precision neutron scattering data in the region $E_n \leq 26$ MeV has put the phenomenological analysis to an increasingly severe test. The conclusion seems to be that average parameters give only average fits to the data. In order to properly reproduce all of the subtleties now evident in differential cross section data, a relatively large number of free parameters must be varied, and not always varied in ways that seem sensible in terms of energy and mass number dependence. In addition, there exist a number of ambiguities in determining the values of such free parameters. Often several potentials of different shape will yield equally good fits to data. For example, there is considerable freedom in the choice of potential depth, radius, and diffuseness, as long as the volume integral of the potential remains invariant. There is also some arbitrariness in partitioning the imaginary potential between volume and surface peaked form factors.

Apart from such phenomenological analyses, it is also possible to approach the optical potential from a more fundamental, microscopic theory. Recently, two such treatments, based upon realistic two-nucleon interactions, have received much attention: the nuclear matter approach of Jeukenne, Lejeune, and Mahaux[4–6] (JLM) starting with Reid's hard core interaction, and the folding model of Brieva and Rook[7–10] using an effective interaction derived in nuclear matter based upon the Hamada-Johnston interaction.

Recent neutron elastic scattering measurements at Ohio University on ^{54,56}Fe at 26 MeV and on ^{54}Fe at 20 and 22 MeV have been combined with previous Ohio measurements on ^{56}Fe at 20 MeV and on ^{54}Fe at 24 MeV and analyzed phenomenologically. These data, together with additional neutron,[11] proton,[12] polarized proton,[13] and polarized neutron[14,15] elastic scattering measurements, are used to test the predictions of both the Brieva-Rook and JLM approaches. The work attempts to provide a comprehensive test of the isospin consistency of these models, which combine nuclear matter calculations with a

local density approximation at low energies.

The two types of microscopic-model calculations predict different potential shapes which are also different from those of the phenomenological model. The significance of these differences is most clearly understood by discussing the characteristics of the potentials in momentum space.

II. EXPERIMENTAL CONDITIONS

The measurements were made using the Ohio University tandem Van de Graaff accelerator and a pulsed beam time-of-flight (TOF) spectrometer. A deuteron beam, pulsed and bunched at a 5 MHz repetition rate with pulse width <1 ns and an average beam current of 3 μA, was incident upon a 3 cm long gas target filled with 1.5 atm of tritium producing monoenergetic neutrons via the ^{3}H (d,n)^{4}He reaction.

The scattering samples, mounted ~ 14 cm from the neutron source, were right circular cylinders of diameter 1.9 cm. The ^{54}Fe sample was 2.4 cm high with a mass of 50.9 g and an isotopic purity of 97.6%. The ^{56}Fe sample was 2.9 cm high with a mass of 63.4 g and an isotopic purity of 99.9%.

The 20 MeV measurement on ^{56}Fe and the 24 MeV measurement on ^{54}Fe were made at the old Ohio University TOF facility with a single 5 cm thick by 20 cm diam NE224 liquid scintillator detector mounted in a massive shield at a flight path of ~ 6.5 m. The 26 MeV measurements on both ^{54,56}Fe and the 20 and 22 MeV measurements on ^{54}Fe were made in the new beam swinger TOF tunnel[16] using a sevenfold array of 10 cm thick by 20 cm diam NE213 detectors and a flight path of 13 m. The new facility provides higher resolution and much lower background owing to the improved shielding and isolation of the detectors from the neutron source.

Pulse shape discrimination was used to eliminate γ rays from the TOF spectra. A monitor detector, at a fixed angle relative to the zero-degree line, observed the direct flux of neutrons from the gas cell. All data were accumulated using the OU8000 on-line computer.[17] The energy resolution obtained in the beam swinger facility was about 430 keV FWHM compared to about 635 keV FWHM for the old TOF facility.

In order to normalize the relative cross sections, the main detector(s) were placed at 0° and the scattering sample removed in order to measure the flux per monitor count which would have been incident upon the scattering sample. In this way the absolute efficiency of the neutron detector(s) need never be known. One merely needs the relative shape of efficiency versus neutron energy, which was measured in a separate experiment.[18]

III. DATA REDUCTION AND CORRECTIONS

The cross sections thus extracted were corrected for dead time. A correction for the variation in detector efficiency was made by multiplying by the ratio

$$\{\text{efficiency}[E_n(0°)]\}/\{\text{efficiency}[E_n(\theta)]\} .$$

The magnitude of this correction never exceeded 10%. An additional correction was made to account for the anisotropy in the neutron source reaction, since the detector(s), when placed at 0°, did not subtend the same solid angle as the scattering sample. This correction was on the order of 1—3 %. Finally, the cross sections were corrected for flux attenuation in the sample, for finite angular geometry due to the size of the sample, and for multiple scattering within the sample using the Monte Carlo computer code MULCAT.[19]

The final corrected data sets are shown in Figs. 1 and 2. The error bars shown, due primarily to counting statistics but also to uncertainties in the 0° flux, range from about 2% at forward angles ($<20°$) to about 10% at extreme backward angles ($>130°$). The error in the overall normalization of the data is $<3\%$.

IV. PHENOMENOLOGICAL ANALYSIS

Standard phenomenological optical model analysis[1] was performed using a conventional Woods-Saxon form factor for the real potential and a combination of a (volume) Woods-Saxon term and a (surface) derivative Woods-Saxon term for the imaginary potential. The spin-orbit potential, which was kept fixed during this analysis, was that due to Becchetti and Greenlees.[2]

Best-fit potentials were obtained individually for each data set by varying seven free parameters in the optical model search code GENOA. These free-geometry searches

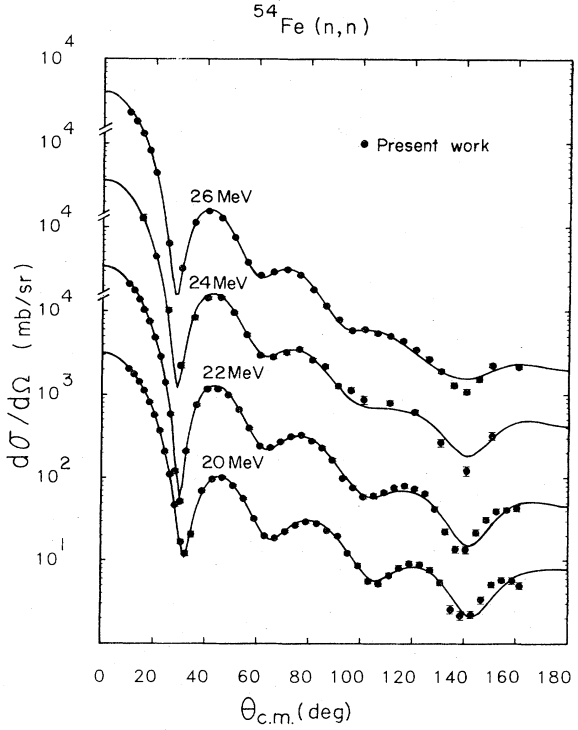

FIG. 1. Average geometry phenomenological optical model fits are compared to measured cross sections for ^{54}Fe(n,n). Optical parameters are given in Table I.

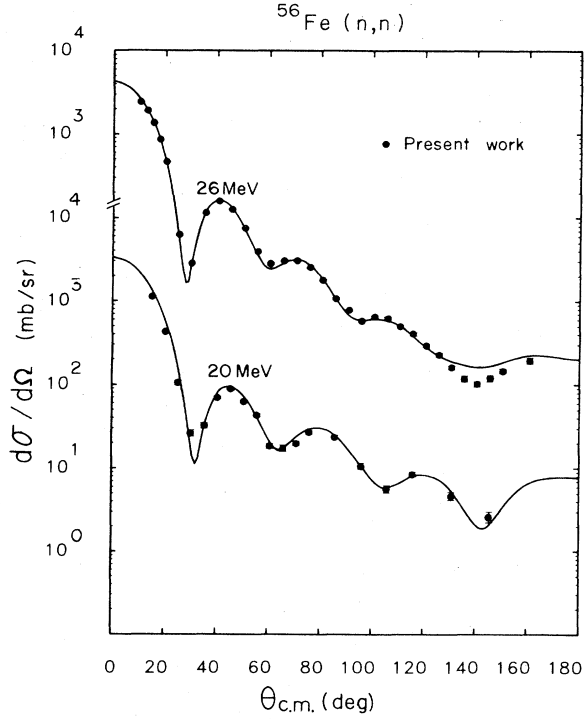

FIG. 2. Average geometry phenomenological optical model fits are compared to measured cross sections for ^{56}Fe(n,n). Optical parameters are given in Table I.

TABLE I. Phenomenological optical model potential depths from an average geometry search with $r_R=1.189$ fm, $a_R=0.6415$ fm, $r_I=1.282$ fm, and $a_I=0.609$ fm. ($V_{SO}=6.2$ MeV, $r_{SO}=1.01$ fm, $a_{SO}=0.75$ fm.)

Nucleus	Energy (MeV)	V (MeV)	W_V (MeV)	W_D (MeV)
^{54}Fe	20	46.18	1.94	5.51
^{54}Fe	22	45.61	1.43	6.01
^{54}Fe	24	43.90	1.92	4.86
^{54}Fe	26	44.18	2.47	5.27
^{56}Fe	20	46.09	2.68	5.08
^{56}Fe	26	43.27	3.07	4.84

were performed in six steps, varying the parameters as follows:

(1) V, W_V, W_D ,

(2) V, a_R, W_V, W_D, r_I ,

(3) V, a_R, W_V, r_I, a_I ,

(4) r_R, a_R, W_V, W_D, r_I ,

(5) r_R, a_R, W_V, r_I, a_I ,

(6) V, W_V, W_D .

After individually fitting each data set, an average geometry was calculated, and the data were fit again, varying only the three potential depths. The quality of these average geometry fits was not significantly different from that of the free geometry searches. The average geometry fits are shown in Figs. 1 and 2, and a summary of all associated parameters is given in Table I.

Predicted differential cross sections were also calculated using the global optical model parameters from set A of Ref. 3. Also included in this analysis were elastic scattering data from both ^{54,56}Fe at 8, 10, 12, and 14 MeV taken by El-Kadi *et al.*[11] The fixed geometry and energy dependent potential depths prescribed by this model provide fairly good agreement with the data at all energies as well as a good representation of the energy dependence of the shape of the cross section. The results for ^{54}Fe are shown in Fig. 3. It should be emphasized that no free parameters or fitting of any kind were involved in this calculation. The results for ^{56}Fe are similar.

V. MICROSCOPIC ANALYSIS

Microscopic optical potentials were calculated from both the Brieva-Rook and JLM approaches, and the differential cross sections thus predicted were compared to the data. The models were also tested by considering proton elastic scattering data in the same energy range as well as available analyzing power measurements.

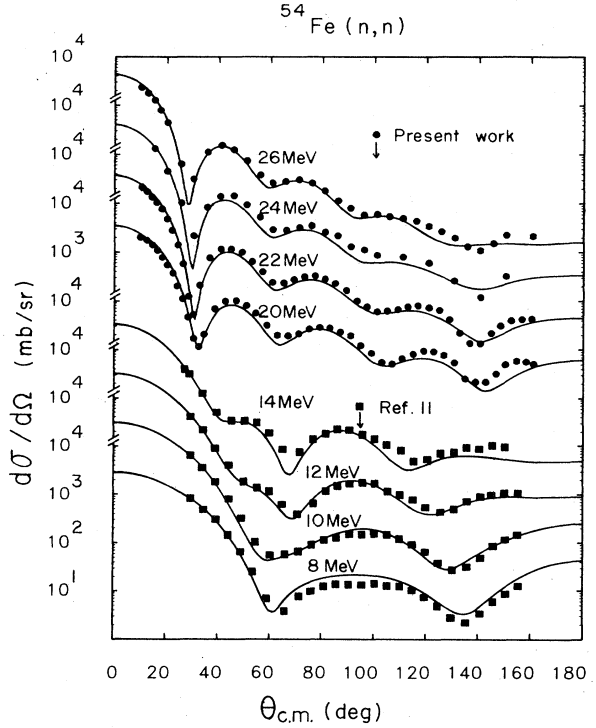

FIG. 3. Global phenomenological optical model calculations using the parameters from set A of Ref. 3 are compared to measured cross sections for ^{54}Fe(n,n).

A. Brieva-Rook interaction

The optical potential for nucleon scattering from spin-zero nuclei contains central and spin-orbit terms:

$$U(r_p)=U_C(r_p)+\vec{U}_{LS}(\vec{r}_p)\times\vec{p}_p\cdot\vec{\sigma}_p \ . \tag{1}$$

In the Brieva-Rook approach,[7–10] infinite nuclear matter calculations based upon the Hamada-Johnston nucleon-nucleon interaction yield the energy and density dependent t matrix, $t(r,k_f,E)$, from which the optical potential in a finite (spherical) nucleus is calculated by folding integrals:

$$U_C(r_p)=\sum_T \epsilon^T \int d^3\vec{r}_t[t_T^{C,D}(r)\rho_T(r_t)+j_0(kr)t_T^{C,E}(r)C(k_F r)\rho_T(r_t)] \ , \tag{2}$$

and

$$\vec{U}_{LS}(\vec{r}_p)=\sum_T \epsilon^T \int d^3\vec{r}_t[\vec{r}t_T^{LS,D}(r)\rho_T(r_t)-(t_T^{LS,E}(k)/k^2)\nabla_{\vec{r}}\delta(\vec{r})\rho(r_t)] \ , \tag{3}$$

where $\vec{r}_p$ and $\vec{r}_t$ refer to the projectile and target nucleons, respectively; t_T^C and t_T^{LS} represent the spin-independent central and the spin-orbit components of the effective interaction, respectively; $\vec{r}=\vec{r}_p-\vec{r}_t$; and ρ_T denotes the ground state density distribution. An isospin representation is assumed with $T=0$ or 1; $\rho_0=\rho_p+\rho_n$; $\rho_1=\rho_n-\rho_p$; and $\epsilon^0=-\epsilon^1=1$ for incident protons and $\epsilon^0=\epsilon^1=1$ for incident neutrons to ensure the correct symmetry dependence of the potentials. The superscripts D and E on t refer to direct and exchange, and the second terms in Eqs. (2) and (3) are standard local approximations for the knockout exchange terms. Here j_0 is a spherical Bessel function, $C(k_F r)$ is a correlation function, $k_F=[3\pi^2\rho_0(R)/2]^{1/3}$ is the local Fermi momentum evaluated at the mean position of the interacting nucleons, $\vec{R}=(\vec{r}_p+\vec{r}_t)/2$, and $k^2=2m[\tilde{E}-\mathrm{Re}U(r_p)]/\hbar^2$ is the square of the local momentum. For incident neutrons $\tilde{E}=E$, where E is the asymptotic energy. In the case of the protons $\tilde{E}$ is corrected for the Coulomb energy, i.e., $\tilde{E}=E-V_C(r_p)$. The question of Coulomb effects comes up again in the evaluation of t which is, in general, a complex function of $\vec{r}$, $\rho_0(R)$, and the energy. The usual prescription is to evaluate t at $\tilde{E}$.[5] As noted below, however, the present work and a related work on ^{208}Pb, where Coulomb effects are more important, indicate that the proper prescription should be to evaluate t at E for both protons and neutrons. A discussion of the physical basis for this prescription is given in Ref. 23.

These integrals contain a "local density approximation" (LDA); i.e., the optical potential for a finite nucleus may be calculated using a t matrix calculated in infinite nuclear matter of density

$$\rho\left[\frac{\vec{r}_p+\vec{r}_t}{2}\right] .$$

The choice of the mean position,

$$\left[\frac{\vec{r}_p+\vec{r}_t}{2}\right] ,$$

in evaluating the density dependence of the effective interaction in the LDA seems physically the most reasonable, although it has not been rigorously justified and must be viewed as somewhat arbitrary. Evaluating the density at either extreme (target or projectile position) changes the shapes of the potentials significantly, particularly for the imaginary potential. This point will be discussed further in Sec. VI.

The densities used in the calculations were obtained as follows: (1) the point proton density was calculated from a Woods-Saxon parametrization of the nuclear charge density of ^{54}Fe (^{56}Fe) obtained from elastic electron scattering[20] by deconvoluting out the finite charge distribution of the proton; and (2) the point neutron density was assumed to be equal to N/Z times the point proton density.

The radial dependence of the Brieva-Rook t-matrix elements has been parametrized by von Geramb[21] as a finite sum of Yukawa terms. This parametrization was used in a folding model computer code to calculate the central potentials for ^{54,56}Fe.

The (real) spin-orbit potentials were calculated by the same program using the Elliott spin-orbit version of the so-called M3Y force.[22] This force is independent of both energy and density.

The optical potentials calculated were used in a spherical optical-model computer program to predict differential cross sections. The calculated potentials were multiplied by two overall normalization parameters, λ_V and λ_W, for the real and imaginary central components, respectively. These parameters were adjusted by least squares for a best fit to the data. The spin-orbit potential was not renormalized in calculations of elastic scattering cross sections, as neutron elastic cross sections are not very sensitive to small changes in V_{SO}, and in any case, the analyzing power calculations show that no large renormalizations are necessary.

The fits thus obtained for ^{54}Fe are shown in Fig. 4. Those for ^{56}Fe were similar. Qualitatively, the fits seem comparable to those obtained by Brieva and Rook for ^{40}Ca.[10] Although the agreement with the data is reasonable, a significant discrepancy is the consistent overestimate of the cross section at forward angles (and thus an overestimate of the total cross section). This is shown most clearly by the new measurements at 20–26 MeV which extend forward to a laboratory angle of 10°.

The ability of the model to calculate proton and neu-

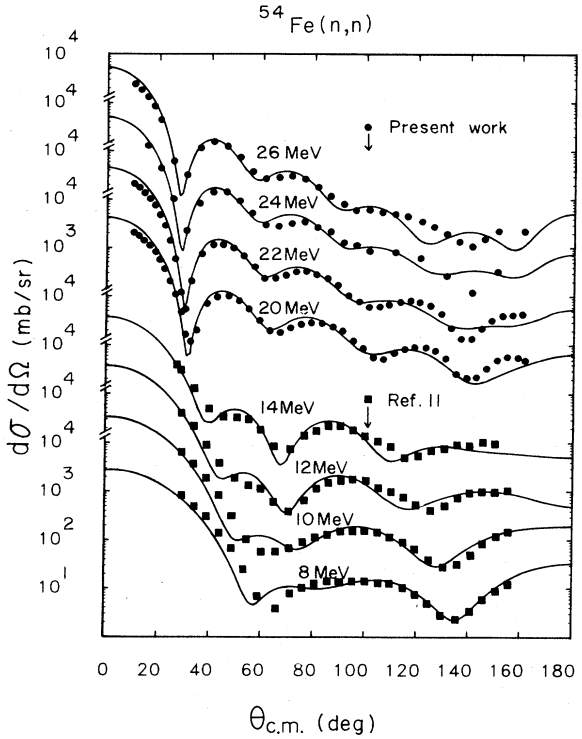

FIG. 4. Brieva-Rook microscopic optical model calculations are compared to measured cross sections for ^{54}Fe(n,n).

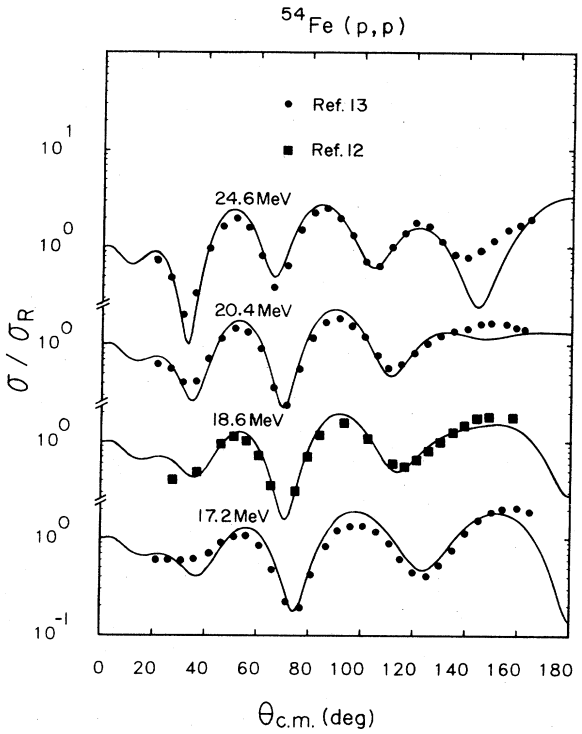

FIG. 5. Brieva-Rook microscopic optical model calculations are compared to measured cross sections for ^{54}Fe(p,p).

tron scattering consistently was tested by using the same procedures to compare with elastic proton scattering data at 18.6 MeV on ^{54}Fe and 19.1 MeV on ^{56}Fe taken by Eccles *et al.*,[12] and polarized proton scattering data on both ^{54,56}Fe at 17.2, 20.4, and 24.6 MeV taken by Van Hall *et al.*[13] The results for the cross section data for ^{54}Fe are shown in Fig. 5. The values of λ_V and λ_W are shown in Fig. 6. The results for ^{56}Fe were virtually identical.

A comment must be made about the analysis of the proton data and the Coulomb correction. In calculating the folding integrals, it was found to be appropriate to use E, not $\tilde{E}$, for the explicit energy dependence of the t matrix, while still including the Coulomb potential in the energy-momentum relationship used in the exchange approximation. By using this prescription, consistency was obtained in the values of λ_V and λ_W for protons and neutrons at similar incident energies. This conclusion was confirmed in recent calculations for ^{208}Pb, where the Coulomb potential is much more significant.[23]

Perhaps most striking, however, is the quality of the results for the proton analyzing power data for ^{54}Fe of Ref. 13 shown in Fig. 7. In this case, both differential cross section and analyzing power data were calculated simultaneously at each energy, and a third parameter, λ_{SO}, was allowed to vary the overall normalization of the spin-orbit potential. However, λ_{SO} did not differ from unity by more than 10%.

Similarly, the model was used to perform calculations for comparison with two sets of elastic neutron analyzing power data: on natural Fe at 24 MeV (Ref. 14) and on

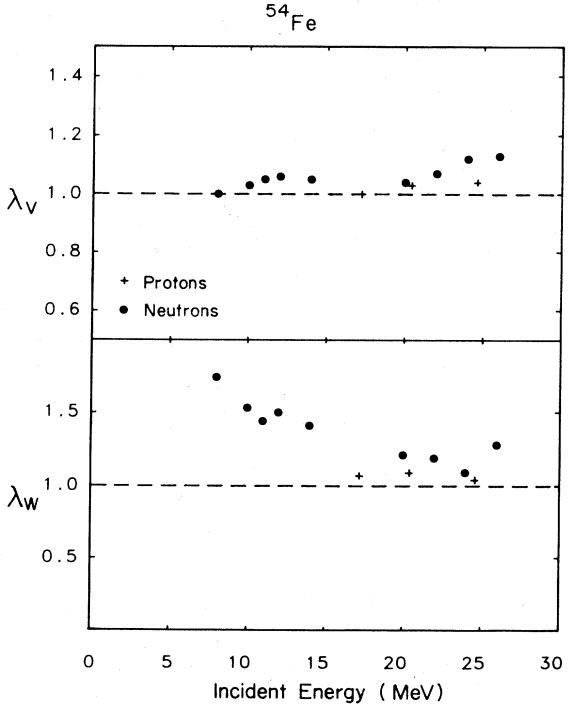

FIG. 6. Normalizing parameters for Brieva-Rook optical potentials.

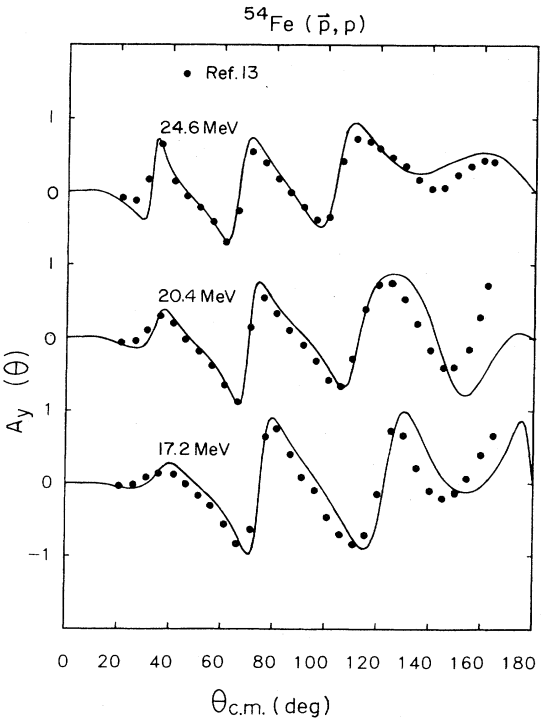

FIG. 7. Brieva-Rook microscopic optical model calculations are compared to measured analyzing powers for ^{54}Fe($\vec{p}$,p).

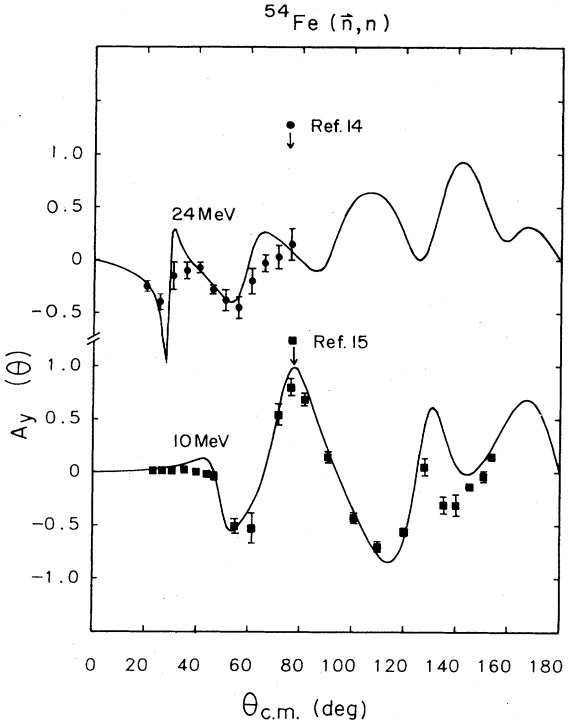

FIG. 8. Brieva-Rook microscopic optical model calculations are compared to measured analyzing powers for ^{54}Fe($\vec{n}$,n).

^{54}Fe at 10 MeV.[15] Again, both analyzing power and cross section data were fit simultaneously (the ^{54}Fe differential cross sections were used at 24 MeV) and again, λ_{SO} never varied from unity by more than 10%. The results are shown in Fig. 8.

B. JLM potential

The calculations of Jeukenne, Lejeune, and Mahaux[4] directly yield the energy and density dependent optical potential in infinite nuclear matter, $U(\rho,E)$. An "improved LDA" is then used to calculate the potential for a finite nucleus: First, by assuming that the optical potential in a nucleus where the density is ρ is the same as the potential in infinite nuclear matter of density ρ (the LDA) and, second, by "smearing" the potential thus calculated, viz.,

$$\tilde{U}(\vec{r}_p,E)=\int U(\vec{r}',E)f(\vec{r}_p-\vec{r}')d\vec{r}' , \tag{4}$$

where

$$f(\vec{r}_p-\vec{r}')=(t\sqrt{\pi})^{-3}\exp[-(\vec{r}_p-\vec{r}')^2/t^2] , \tag{5}$$

where the parameter t reflects the finite range of the nuclear force. JLM use a value $t_R=1.2$ fm for the real potential and suggest that perhaps a larger value might be appropriate for t_I (for the imaginary potential).[5] JLM also suggest a second way of performing the smearing, namely,

$$\tilde{U}(\vec{r}_p,E)=\frac{U(\vec{r}_p)}{\rho(\vec{r}_p)}\int \rho(\vec{r}')f(\vec{r}_p-\vec{r}')d\vec{r}' . \tag{6}$$

The relationship between these prescriptions may be clarified by defining an "effective interaction" between projectile and target particle

$$\{U[\rho(\vec{r}_x)]/\rho(\vec{r}_x)\}f(\vec{r}_p-\vec{r}_t) ,$$

where $\vec{r}_x$ remains to be specified. Then this "interaction" is folded with the density to yield

$$\tilde{U}(\vec{r}_p)=\int \rho(\vec{r}_t)\frac{U[\rho(\vec{r}_x)]}{\rho(\vec{r}_x)}f(\vec{r}_p-\vec{r}_t)d\vec{r}_t . \tag{7}$$

Choosing $\vec{r}_x=\vec{r}_t$ yields the first of the JLM prescriptions, whereas $\vec{r}_x=\vec{r}_p$ yields the second. In an attempt to apply the JLM approach in a manner as nearly equivalent to the Brieva-Rook as possible, we have made a third choice,

$$\vec{r}_x=\frac{\vec{r}_p+\vec{r}_t}{2} .$$

As with the Brieva-Rook calculations, the differences among the three choices are significant and will be illustrated later. A further modification of the JLM potential has been incorporated by multiplying the imaginary potential (before folding) by an effective mass factor [the k mass, Eq. (29) of Ref. 5]. The necessity for this correction has been pointed out by Negele and Yazaki[24] and by Fantoni *et al.*[25] Although preliminary calculations with the

original version of the JLM model showed that $t_R = t_I = 1.2$ were satisfactory for the range parameters, these values yielded total neutron cross sections that were $\approx 15\%$ too large in the 20 MeV region with the "mean-position" version of the LDA and the effective mass correction. The total cross section proved to be very sensitive to the values of the range parameters, with $t_R = t_I = 1.0$ yielding much improved results; these values were used in all of the calculations shown. The densities were identical to those used in the Brieva-Rook calculations. The spin-orbit potential used was again from the Elliott M3Y force.[22]

All of the aforementioned neutron and proton cross sections were fit using JLM potentials, again with only the two overall normalization parameters λ_V and λ_W. The results for the neutron cross sections for ^{54}Fe are shown in Fig. 9. Partly because of the adjustment of the range parameters, the agreement at the forward angles is very good, as are the estimates of the total cross section throughout the energy range. The results for the proton cross sections for ^{54}Fe are shown in Fig. 10, and the values of λ_V and λ_W for all cases are shown in Fig. 11. As for the Coulomb correction, when evaluating $U(\rho,E)$ for protons, the value $\tilde{E}$ was consistently used as prescribed in Ref. 5. As demonstrated in Fig. 11, this led to consistency in the values of λ_V and λ_W for neutrons and protons at similar energies.

The proton and neutron analyzing power data were also compared with the predictions of the JLM potentials. Again, as for the calculations based on the Brieva-Rook approach, the parameter λ_{SO} was allowed to vary in order to improve the simultaneous fit to $(d\sigma/d\Omega)(\theta)$ and $A_y(\theta)$ values. The results were comparable, and again the variation of λ_{SO} from unity was on the order of 10% or less.

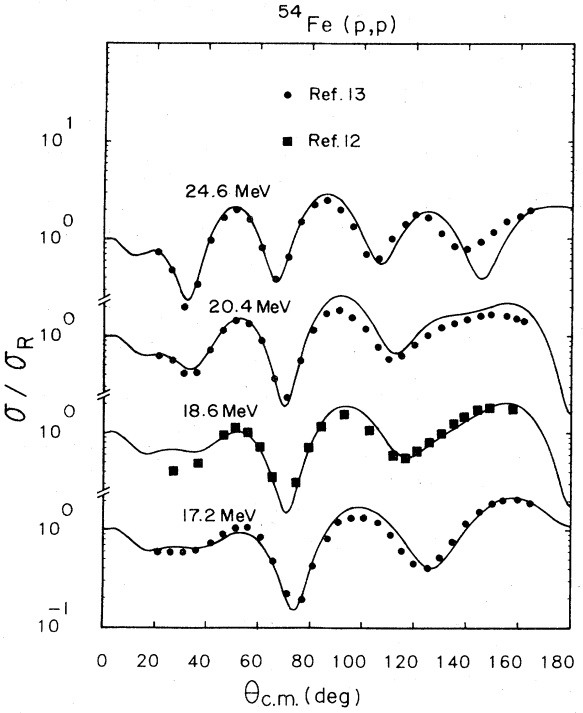

FIG. 10. JLM microscopic optical model calculations are compared to measured cross sections for ^{54}Fe(p,p).

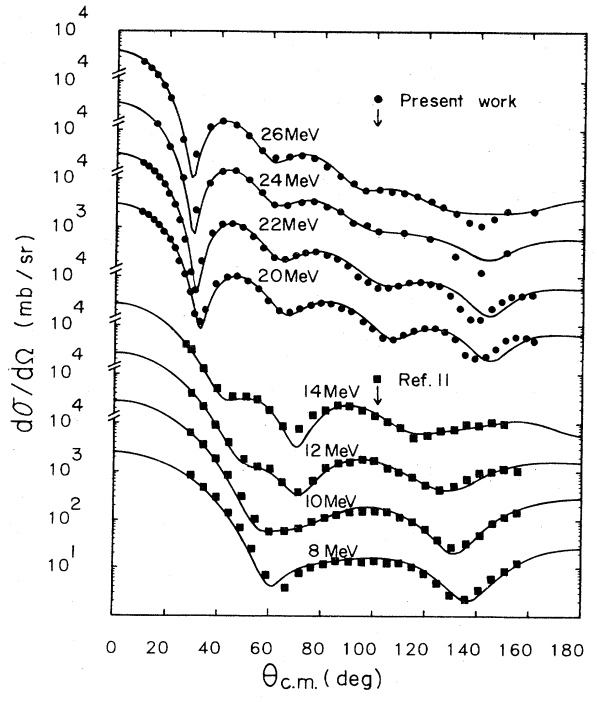

FIG. 9. JLM microscopic optical model calculations are compared to measured cross sections for ^{54}Fe(n,n).

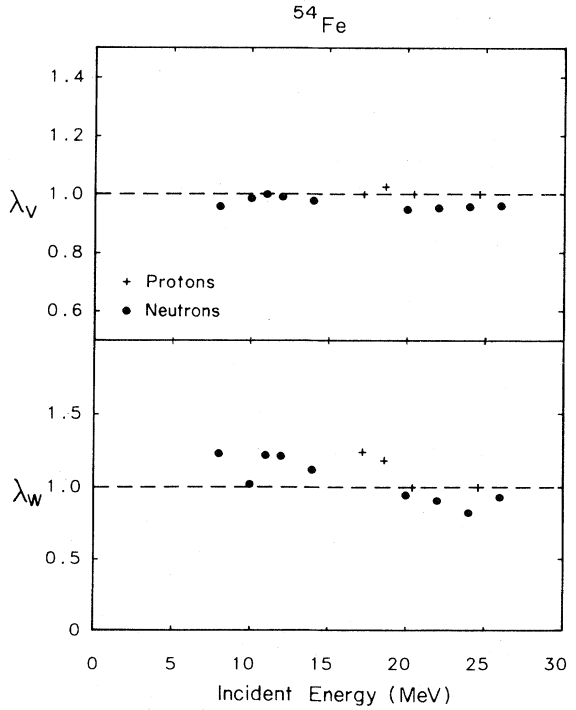

FIG. 11. Normalizing parameters for JLM optical potentials.

VI. COMPARISON OF POTENTIALS

Since the two microscopic models compared systematically in this work are based on different representations of the free two-nucleon interaction and result from different numerical techniques as well as the method of applying a local density approximation, it is noteworthy that the calculated scattering cross sections are so similar. In this section we attempt to understand to what features of the optical potentials the scattering is sensitive.

A. Coordinate-space representation

Figures 12 and 13 show the microscopic optical potentials for 24 MeV neutrons on ^{54}Fe for the two models, along with the phenomenological potential. For each of the microscopic models, separate curves are shown for the three prescriptions of evaluating the density dependence (projectile, target particle, and mean position). Also shown in each figure is the phenomenological potential corresponding to the cross sections in Fig. 1. There are marked shape differences among the different models as well as among the prescriptions for applying the LDA. The sensitivity to the latter is particularly evident for the imaginary potential, which is a consequence of the strong density dependence of the imaginary potential in this energy range due to Pauli-blocking effects. Although the well-known transition from a surface-peaked imaginary potential at low energies to a volume form at high energies

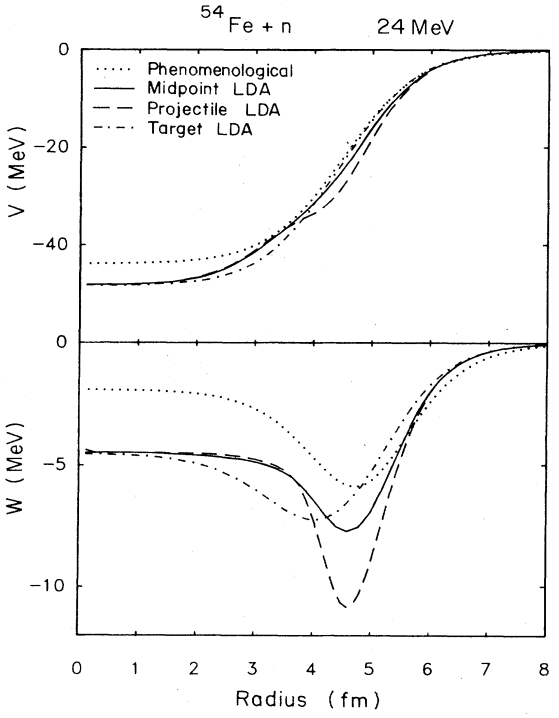

FIG. 13. Coordinate-space representations of JLM microscopic optical potentials for ^{54}Fe+n at 24 MeV calculated with the three different methods of applying the LDA are compared with the best-fit phenomenological potential for the same case.

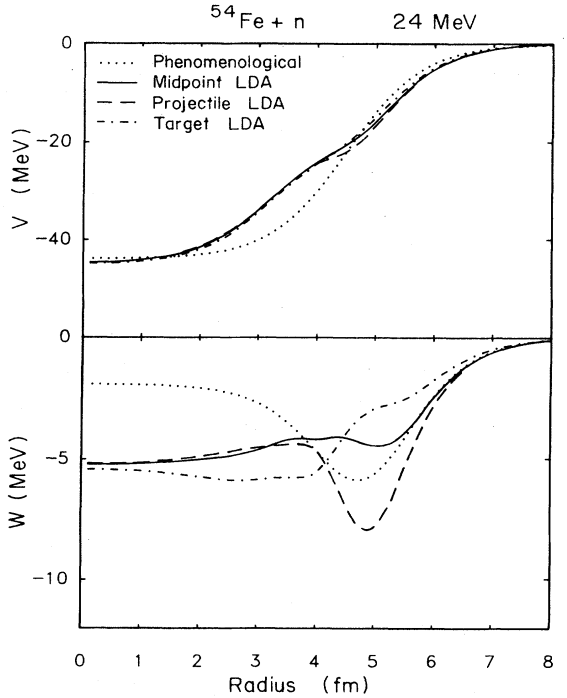

FIG. 12. Coordinate-space representations of Brieva-Rook microscopic optical potentials for ^{54}Fe+n at 24 MeV calculated with the three different methods of applying the LDA are compared with the best-fit phenomenological potential for the same case.

is qualitatively reproduced in both models, the size and position of the surface peak are dependent on the method of applying the LDA. Significantly, however, when renormalization of the potentials is allowed (by varying λ_V and λ_W) the calculated scattering cross sections from the various potentials are rather similar. It is not obvious from their coordinate space representations that this should be so, nor is there a clear correlation between differences in the scattering and specific features of the potentials.

Table II summarizes the real and imaginary volume integrals and mean-square radii of all the potentials used in the various analyses. Qualitatively, the volume integrals of the real potentials from the phenomenological and JLM calculations have the monotonically decreasing energy dependence expected,[1] while the Brieva-Rook has a peak at about 12 MeV. On the other hand, the volume integrals of the imaginary potentials from the phenomenological and the Brieva-Rook calculations have the expected peak around 15 MeV,[1] while those of JLM do not. And while the mean square radii of the phenomenological real potentials are close to those for JLM, those of the phenomenological imaginary potentials are closer to the Brieva-Rook potentials.

B. Momentum-space representation

More insight may be gained by examining the same potentials in momentum space, calculated according to

TABLE II. Volume integrals per nucleon and mean square radii of optical potentials from all analyses. The tabulated volume integrals per nucleon for the two microscopic models include the normalization factors λ_V and λ_W such as those from Figs. 6 and 11.

		Phenomenological				Brieva-Rook				JLM			
Reaction	Energy (MeV)	J_R/A (MeV fm^3)	$\langle r^2\rangle_R$ (fm^2)	J_I/A (MeV fm^3)	$\langle r^2\rangle_I$ (fm^2)	J_R/A (MeV fm^3)	$\langle r^2\rangle_R$ (fm^2)	J_I/A (MeV fm^3)	$\langle r^2\rangle_I$ (fm^2)	J_R/A (MeV fm^3)	$\langle r^2\rangle_R$ (fm^2)	J_I/A (MeV fm^3)	$\langle r^2\rangle_I$ (fm^2)
^{54}Fe(n,n)	8	425.2	17.8	101.5	27.3	435.4	19.1	110.4	26.2	426.6	17.8	120.5	26.1
	10	423.9	17.8	99.7	28.3	441.9	19.2	114.7	27.3	432.3	17.8	100.8	25.6
	12	416.3	17.8	102.4	28.0	444.4	19.2	124.5	27.7	428.0	17.7	96.9	22.8
	14	407.7	17.8	103.0	28.6	427.8	19.1	122.0	27.6	415.6	17.7	95.5	23.1
	20	390.5	17.8	97.0	27.4	389.2	18.8	105.4	26.3	385.1	17.5	91.8	23.5
	22	385.7	17.8	98.7	28.0	390.6	18.7	103.5	25.8	381.3	17.5	90.4	23.5
	24	371.3	17.8	87.6	27.2	395.3	18.7	94.2	25.4	376.9	17.4	83.4	23.4
	26	373.6	17.8	99.1	26.9	391.9	18.6	111.6	25.0	372.4	17.4	95.8	23.3
^{56}Fe(n,n)	8	426.8	17.8	91.9	27.7	438.3	20.0	103.4	27.3	433.2	18.7	105.6	27.5
	10	412.8	17.8	95.4	28.2	433.8	20.1	116.4	28.5	423.2	18.7	102.2	27.0
	12	409.4	17.8	98.2	28.9	444.9	20.1	119.9	29.0	421.4	18.6	92.7	24.0
	14	403.6	17.8	100.5	28.5	434.1	20.0	127.7	28.9	416.1	18.6	96.6	24.3
	20	388.2	17.8	97.3	27.2	401.3	19.7	122.0	27.6	391.3	18.5	98.8	24.7
	26	364.4	17.8	98.0	26.8	395.7	19.5	115.9	26.2	371.6	18.3	97.7	24.6

$$U(q)=\int_0^\infty r^2 dr\, j_0(qr)U(r)\ . \tag{8}$$

The differences in potential shape due to the three methods of applying the LDA are much less pronounced in the q-space representation of the potentials. Figure 14 shows the squares of the real and imaginary parts of the 24 MeV ^{54}Fe potentials for the phenomenological, Brieva-Rook, and JLM models (where the "mean position" LDA has been used for both microscopic models). It might be expected that the q-space representation of the potentials is more closely related to the scattering cross sections since in the plane-wave Born approximation (PWBA) limit, the cross section is simply proportional to $V^2(q)+W^2(q)$. It is also well known that the properties of an optical potential most accurately determined by scattering are the volume integral J and mean-square radius $\langle r^2\rangle$. Indeed, these quantities are fixed by the value and curvature of $U(q)$ at $q=0$, since

$$J=4\pi U(q=0)$$

and

$$\langle r^2\rangle=-3U''(q=0)/U(q=0)\ .$$

However, since elastic scattering at the energies in the present work is far from the PWBA limit, the significance of distortion effects must be considered. In Fig. 15 the upper curves (a), (b), and (c) correspond to cross sections calculated (including distortion) from the real part of the JLM potential of Fig. 14, while the lower three correspond to PWBA calculations using the same potential. The dotted lines for each curve correspond to calculations made with: (a) an artificial, constructive disturbance placed on the first maximum of $V(q)$; (b) such a disturbance placed on the second maximum; and (c) on the third maximum. It is apparent that the distortion effects are drastic; the number and position of the maxima and minima in the exact calculation are different from the PWBA result. Nevertheless, an important feature of the PWBA result is

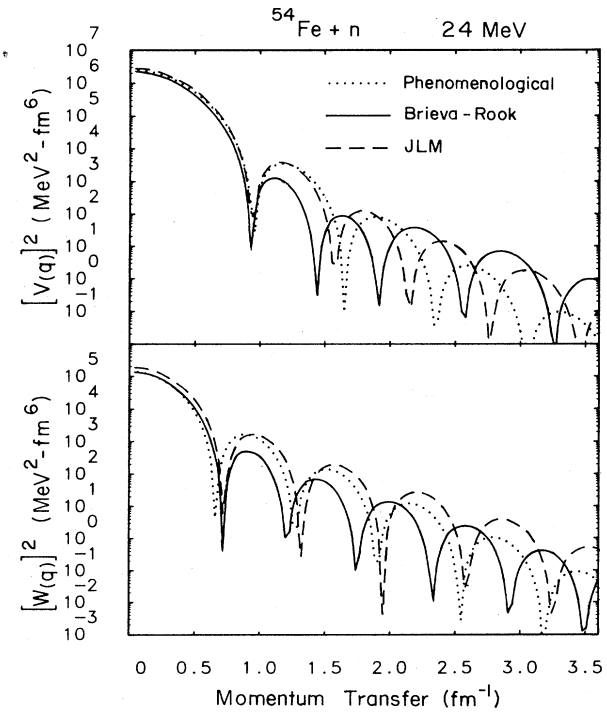

FIG. 14. Momentum-space representations of both Brieva-Rook and JLM microscopic optical potentials (calculated with the midpoint LDA) for ^{54}Fe + n at 24 MeV are compared with the best-fit phenomenological potential for the same case.

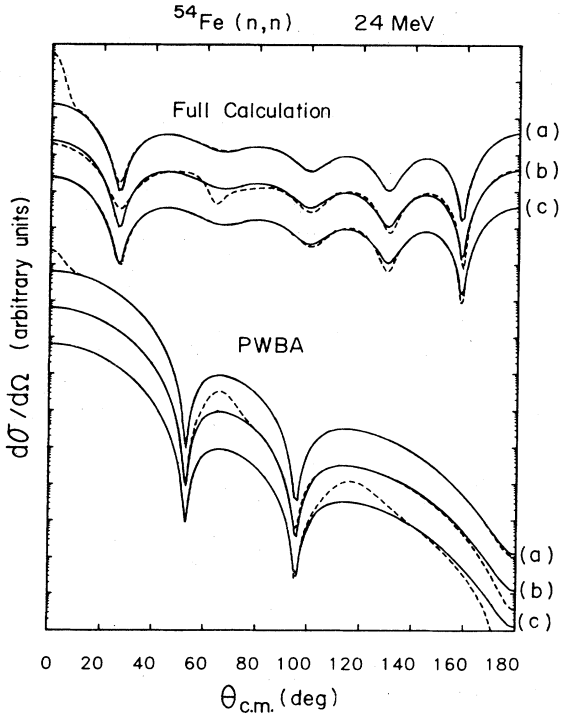

FIG. 15. Dashed lines represent differential cross sections for ^{54}Fe(n,n) at 24 MeV calculated from the real part of the JLM potential of Fig. 14 in both PWBA and full distorted-wave calculation with (a) an artificial disturbance on the first maximum of $V(q)$; (b) such a disturbance placed on the second maximum; and (c) on the third maximum. Solid lines represent calculations with no disturbances.

preserved: A disturbance at a given angle in the PWBA calculation has its maximum impact in the same angular region in the full calculation. It is also apparent from Fig. 15 that the importance of the successive lobes of $V^2(q)$ in determining the scattering diminishes rapidly with increasing q. The disturbance at the third lobe has rather little influence on the cross section in the full calculation, and its effects are confined to large scattering angles. Disturbances at higher maxima, which are beyond the value of q corresponding to 180° scattering (2.11 fm^{-1}), proved to have a negligible effect on the angular distribution.

We may now attempt to correlate features in the calculated model cross sections with those in the q-space potentials. The most obvious deviations among the potentials are between the Brieva-Rook and the phenomenological models. In particular, the second maximum of the real potential is shifted with respect to the phenomenological potential, and is lower in magnitude (Fig. 14). The shifting of the q-space maxima is a result of the unusual shape of the r-space potential (Fig. 12). The systematic overprediction of the zero-degree differential cross sections (Fig. 4) is likely to be correlated with this feature of the q-space potential since Fig. 15 shows that adding strength in the region of the second maximum not only changes the behavior of the cross section in the region 50°–100°, but also lowers the cross section at 0°. The Brieva-Rook and phenomenological real potentials are completely out of phase in the third maximum ($q \geq 1.5$ fm^{-1}), and it is therefore not surprising that the predictions of the Brieva-Rook calculations compare poorly with the data (Fig. 4) at back angles ($\geq 120°$). Fits to the 24 MeV data are better with the JLM model (Fig. 9), and this can be seen in the momentum-space potential plots as a reasonably close agreement between the shapes of the JLM and phenomenological potentials in the first two maxima. Deviations beyond the second maximum, while not as severe as for the Brieva-Rook model, nevertheless show up as back-angle discrepancies in comparison with the data.

The strong sensitivity of the total cross section to the range parameters in the JLM model, noted in Sec. V, may be understood from the behavior of the q-space potential. An overestimate of the total cross section was rectified by decreasing the range parameters; decreasing the range parameters increases the relative height of the second q-space maximum of the real potential, which in turn lowers the zero-degree cross section (see Fig. 15). According to Wick's limit

$$[d\sigma/d\Omega(0°) \propto \sigma_{\text{tot}}^2] ,$$

the total cross section is correspondingly lowered.

VII. DISCUSSION

The phenomenological model fits to the individual data sets (with several free parameters) provide an excellent representation of the data. The global phenomenology provides average fits as expected, and does a good job of describing the energy dependence of the differential cross section from 8 to 26 MeV, but it fails to describe the details of each distribution adequately.

Overall, predictions of the two microscopic models are remarkably good considering the small number of free parameters, the very basic nature of the calculations, and the approximations used (e.g., the LDA). The JLM model yields better predictions of the neutron differential cross sections as well as the neutron total cross section. Figure 16 shows the predictions of the two models for ^{56}Fe compared to a recent evaluation of measured total cross sections on natural Fe.[26] The ability of the microscopic model using the Elliott M3Y spin-orbit force to predict elastic analyzing powers is also quite impressive.

An important indication of the success of the two models is the behavior of the parameters λ_V and λ_W. In all cases λ_V is near unity (Figs. 6 and 11) with very little indication of an energy dependence, which supports the validity of the models. However, the shapes of the real potentials are quite different for the two models, and the comparison of the microscopic potentials with the phenomenological one in q space suggests that the JLM potential should yield better agreement with the data, as is the case. Although adjusting the range parameter in the JLM calculations is certainly responsible for part of the improved agreement, the qualitative differences between the potentials in the range beyond $q = 1.2$ fm^{-1} (to which the data are still sensitive) are not altered by reasonable

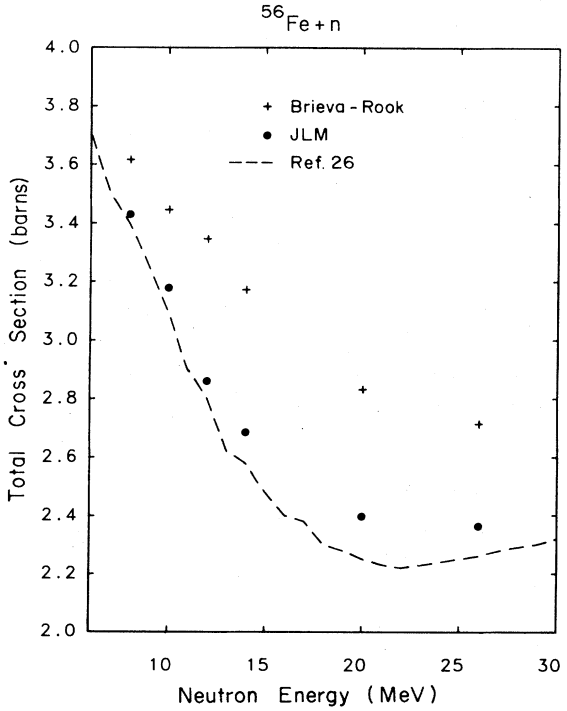

FIG. 16. Neutron total cross sections predicted by both Brieva-Rook and JLM calculations for ^{56}Fe + n are compared with an evaluation of experimental total cross sections on natural Fe from Ref. 26.

variations of the range parameter. The difference in potential shapes may possibly be associated with the fact that the volume integrals of the tabulated Brieva-Rook interaction do not show a smooth behavior as a function of Fermi momentum (i.e., of the density) for either the real or imaginary potential. The overestimate of the total cross section in the Brieva-Rook calculations is not necessarily due to an inaccuracy in the ranges of the interaction, as the total cross section is also dependent upon the accuracy of the density dependence in the force and the validity of the LDA.

The imaginary normalizing parameters λ_W show that the JLM potentials require much less change of the renormalization with energy than the Brieva-Rook; the JLM potentials also yield a surface-to-volume ratio more in the direction of the phenomenological analysis. At the lowest energies (≤ 10 MeV), both types of microscopic potential predict substantial volume absorption, whereas phenomenological potentials tolerate very little volume absorption for an optimal fit.

In conclusion then, the results of the microscopic analysis, while not perfect, are encouraging, considering their very basic origins and the small number of free parameters used. Further efforts should be made in refining this type of model, for it does seem that such microscopic calculations may eventually remove the ambiguities inherent in a purely phenomenological analysis.

ACKNOWLEDGMENTS

We are indebted to Mr. R. G. Kurup, Mr. A. S. Meigooni, and Dr. G. Randers-Pehrson for help in conducting the recent measurements, and to Dr. T. S. Cheema for the reduction of the 20 MeV ^{56}Fe(n,n) data. This work was supported by the National Science Foundation under Grants Nos. PHY-8108456 and PHY-8122131 and by the US Department of Energy under Contract No. W-7405-ENG-48.

[1]J. Rapaport, Phys. Rep. 87, 25 (1982).
[2]F. D. Becchetti and G. W. Greenlees, Phys. Rev. 182, 1190 (1969).
[3]J. Rapaport, V. Kulkarni, and R. W. Finlay, Nucl. Phys. A330, 15 (1979).
[4]J. P. Jeukenne, A. Lejeune, and C. Mahaux, Phys. Rep. 25C, 83 (1976).
[5]J. P. Jeukenne, A. Lejeune, and C. Mahaux, Phys. Rev. C 16, 80 (1977).
[6]A. Lejeune, Phys. Rev. C 21, 1107 (1980).
[7]F. A. Brieva and J. R. Rook, Nucl. Phys. A291, 299 (1977).
[8]F. A. Brieva and J. R. Rook, Nucl. Phys. A291, 317 (1977).
[9]F. A. Brieva and J. R. Rook, Nucl. Phys. A297, 206 (1978).
[10]F. A. Brieva and J. R. Rook, Nucl. Phys. A307, 493 (1978).
[11]S. M. El-Kadi *et al.*, Nucl. Phys. A390, 509 (1982).
[12]S. F. Eccles, H. F. Lutz, and V. A. Madsen, Phys. Rev. 141, 1067 (1966).
[13]P. J. Van Hall *et al.*, Nucl. Phys. A291, 63 (1977).
[14]C. Wong, J. D. Anderson, J. W. McClure, and B. D. Walker, Phys. Rev. 128, 2339 (1962).
[15]C. E. Floyd in *Polarization Phenomena in Nuclear Physics—1980 (Fifth International Symposium, Santa Fe),* Proceedings of the Fifth-International Symposium on Polarization Phenomena in Nuclear Physics, AIP Conf. Proc. No. 69, edited by G. G. Ohlson, R. E. Brown, N. Jarmie, M. W. McNaughton and G. M. Hale (AIP, New York, 1981).
[16]R. W. Finlay, C. E. Brient, D. E. Carter, A. Marcinkowski, S. Mellema, G. Randers-Pehrson, and J. Rapaport, Nucl. Instrum. Methods 198, 197 (1982).
[17]D. E. Carter, Nucl. Instrum. Methods 160, 165 (1979).
[18]S. Mellema and G. Randers-Pehrson, Bull. Am. Phys. Soc., 27, 629 (1982).
[19]W. E. Kinney, Oak Ridge National Laboratory Report ORNL-TM-2052 (1968).
[20]C. W. De Jager, H. De Vries, and C. De Vries, At. Nucl. Data Tables 14, 79 (1974).
[21]H. V. von Geramb (private communication).
[22]G. Bertsch, J. Borysowicz, H. McManus, and W. G. Love, Nucl. Phys. A284, 399 (1977).
[23]F. S. Dietrich *et al.*, Phys. Rev. Lett. 51, 1629 (1983).
[24]J. W. Negele and K. Yazaki, Phys. Rev. Lett. 47, 71 (1981).
[25]S. Fantoni, B. L. Friman, and V. R. Pandharipande, Phys. Lett. 104B, 89 (1981).
[26]E. D. Arthur and P. G. Young, Los Alamos Scientific Laboratory Report LA-8626-MS, 1980.